5. DISCUSSION

5.1. SSM-HPDC

5.1.1. Rheoprocessing

The rheoprocessing step during SSM-HPDC produces relatively coarse globular primary α-Al grains (Fig. 4.5). The coarse α-Al primary globular structure of 60-70μm diameter (Table 4.1 and Fig. 4.55(a)) is typical for SSM-processed A356/7 alloys – see for instance Fig. 2.15 from Nafisi et al [56]) where even coarser average globule circular diameters of 81μm in A356 without Ti and B, and with a diameter of 78μm in A356 with Ti and B, was found. Birol [13,14] postulated that the favourable impact of the globular structure (presumably lower surface area/volume) of the globular primary α-Al is offset by this relatively coarse structure in SSM-processed alloys and that this is the main cause of the comparable heat treatment response between globular and dendritic A356/7 alloys. However, this study has considered the effects of both fine (Fig. 4.55(b)) and relatively coarse (Fig. 4.59) dendritic microstructures in comparison with the globular SSM-processed microstructure and found that the strength (or hardness) in the T6 temper condition is controlled primarily by the Mg-content of the alloy (see Fig. 4.62), rather than primary α-Al microstructure.

5.1.2. High pressure die casting

The relatively high cooling rates that are achieved with HPDC (Fig. 4.4) play an important role in the microstructural evolution and heat treatment response of these alloys. Figure 4.4 illustrates that cooling rates of ~ 18^{o}C/s are estimated during the initial stages of solidification of SSM-HPDC castings and this results in modification of the eutectic component, even at low Sr levels of only 14 ppm (Fig. 4.6). It also enables rapid spheroidisation of the eutectic silicon particles during solution treatment (Fig. 4.8 and also see section 5.2.1).

The high cooling rates additionally retain a relatively high quantity of solutes in solid solution which causes a decrease in the time needed for solution treatment (see section 5.2.2) and allows a relatively high aging response for the T5 temper condition (see section 5.5).

5.2. Solution heat treatment

5.2.1. Spheroidisation of eutectic Si

The purpose of modification is to enable rapid spheroidisation of the silicon particles during solution treatment, with the advantage of high cooling rates during SSM-HPDC being that low Sr levels of only 14 ppm are required (Fig. 4.8) as compared to about 200 ppm that is necessary in permanent mould and investment cast A356/7 [9].

The cube of the change in mean diameter of the Si eutectic particles is in reasonable direct proportion to the solution treatment time (Fig. 4.11) as predicted by Lifshitz-Slyozov-Wagner (LSW) for the diffusion controlled coarsening of a second phase. Ogris has also shown that coarsening of the eutectic Si-particles follows the Lifshitz-Slyozov-Wagner (LSW) theory of Ostwald ripening [6]. However, in the study of Ogris [6], the mean diameter of Si-particles was incorrectly plotted as a function of $t^{1/3}$. This implies that the initial diameter (D_o) in the LSW theory is zero, which is obviously not the case (Fig. 4.10). The Si-particles are not spheroidised at the start of solution heat treatment, but they do not have a zero size. The slight deviation from linearity at short solution treatment times in this study in Fig. 4.11 is therefore most likely related to the fact that the Si particles do not commence growth immediately as spherical particles, but firstly have to undergo spheroidisation before growth can continue through LSW coarsening. This observation is supported by the better linear fit in Fig. 5.1, by rather starting the LSW-graph only at t = 30 minutes where it is known that spheroidisation has occurred (Fig. 4.10), and using D_o = 1.12 μm from Table 4.4. Further support for this argument can be found in the work of Parker and co-workers [69], who also did not consider spheroidisation as part of the coarsening process.

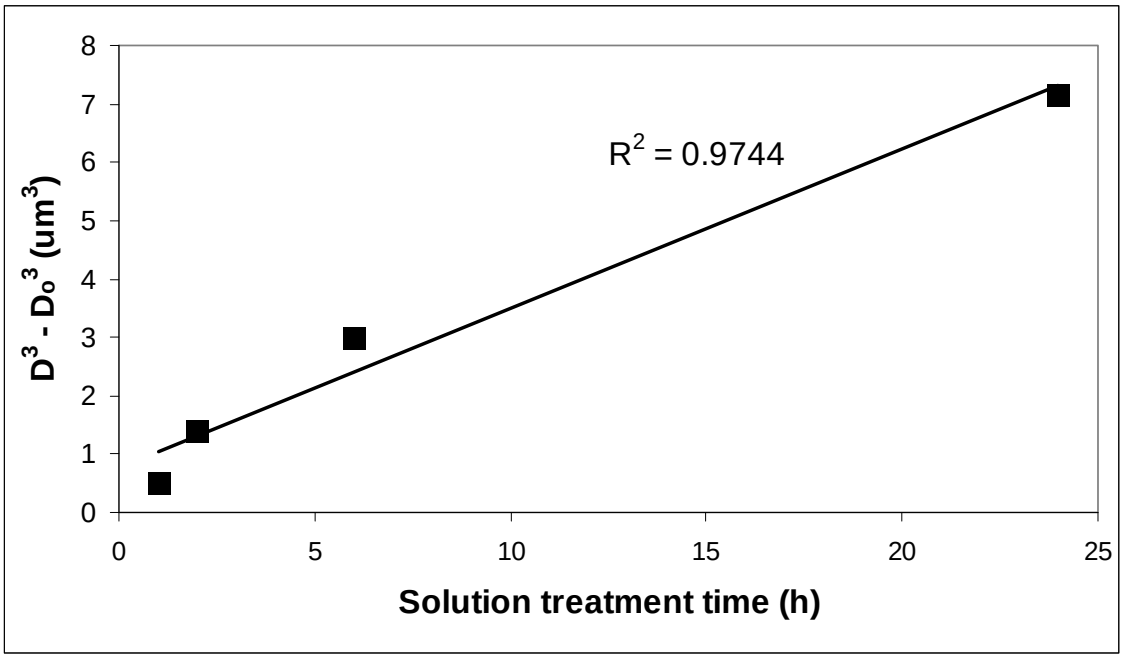

Figure 5.1: The cube of the change in mean diameter of the Si eutectic particles as a function of solution treatment time at 540°C using a starting diameter (D_o) of spheroidised Si after 30 minutes of solution treatment.

Spheroidisation of the eutectic Si occurs rapidly at 540°C (Fig. 4.10), with Parker and co-workers [69], as well as Ogris [6] suggesting that it is complete in less than 10 minutes. The eutectic Si-particles in unmodified alloys do not spheroidise, even after long times at 540°C (Fig. 4.9). The long solution treatment times (4-10 h) frequently specified for these alloys (Table 2.6) most likely cater for unmodified alloys and would be an energy and production restriction for modified alloys, provided that complete solutionising of solutes can also occur in shorter times [58].

5.2.2. Dissolution of solutes and reduction of microsegregation

Taylor et al [47] and Rometsch et al [68] showed that dissolution of Mg_2Si particles and homogenisation of the concentration profiles are complete within one hour at 540°C for both A356 and A357. In spite of these short reported times (and the rapid spheroidisation of the Si-particles in modified alloys), times of 4-10 h are specified for these alloys at 540°C (Table 2.6). Rosso and Actis Grande [90] proposed that a solution heat treatment of 1 hour at 540°C is sufficient to obtain a high level of properties in the T6 temper of SSM-processed A356. According to Dewhirst [12], the optimum solution treatment time for SSM-processed A356 at 540°C is 4 h. Birol [13]

suggested that a solution treatment time of at least 2 h at 540^{o}C is required to obtain maximum hardness after artificial aging in the SSM-processed alloy F357 (Fig. 2.36). A large variation in suggested solution treatment times is therefore found in the literature for SSM-processed alloys A356/7. The tensile results in Table 4.5 of SSM-HPDC alloy F357 with a high Mg-content of 0.62% Mg in this study show that a high level of properties in the T6 temper condition can be obtained after only 30 minutes of solution treatment at 540^{o}C. This is in contradiction to the results of Birol in Fig. 2.36 [13] and is most likely caused by the fact that HPDC was used in this study, resulting in higher cooling rates during solidification (Fig. 4.4) than achieved by Birol in his study. These high cooling rates achieved with HPDC promotes enhanced solutionising before heat treatment commences and result in shorter times being required.

5.2.3. Impact strength

Another important consideration to optimise solution treatment time is the impact strength of the alloys that can be achieved (Table 4.6). Zhang et al [67] found that shorter solution treatments than the standard 6 hours resulted in lower impact strengths for permanent mould cast A356-T6. This was attributed to the smaller interparticle Si-spacing after shorter solution treatments, which assisted with crack growth. However, Ogris [6] showed that the impact strength for thixoformed A357-T6 was better using only 3 minutes solution treatment compared to 12 hours. This was postulated to be due to the fact that the Si was three dimensionally separated after 3 minutes at 540^{o}C, whereas longer times caused the silicon to agglomerate and form large interconnected silicon crystals. This hypothesis seems unlikely as the agglomeration of the Si should rather form large crystals that are not interconnected as the Si- interparticle spacing increases due to coarsening. Similar impact properties were obtained after a solution treatment of 1 h rather than 6 h for each composition in this study in the T4 and T6 temper conditions (Table 4.6). However, it was also shown in Fig. 4.13 that the strength of the alloy plays a more important role in the impact strength in the T4 and T6 temper conditions than the solution treatment time. The higher impact strength for thixormed A357-T6 found by Ogris [6] using only 3 minutes solution treatment time rather than 12 h, is therefore most likely a “strength effect” rather than a “Si-interparticle spacing effect”. Solution treatment for only 3 minutes does not allow complete dissolution of strengthening solutes, resulting in a lower strength in the T6 temper condition (YS = 240 MPa, UTS = 325 MPa) than

after 12 h solution treatment (YS = 312 MPa, UTS = 358 MPa) [6]. The lower strength of the 3 minute solution treated sample will, however, improve the impact properties of the alloy according to Fig. 4.13.

In addition, Figure 4.53 also indicates that good mechanical properties in the T4 and T6 temper conditions can be achieved in a larger, more complex casting such as an automotive brake calliper by using shorter solution treatment times.

Conclusion: Considering the processes of spheroidisation of eutectic Si-particles, dissolution of solutes, reduction of microsegregation, achieving the optimum tensile and impact properties, as well as the size of the casting, the optimum solution treatment parameters for SSM-HPDC alloys A356 and F357 are suggested to be 540^{o}C for 1 h.

5.3. Quench after solution treatment

Slow quench rates after the solution heat treatment can reduce the problems of distortion and residual stresses, but also result in a loss of strength after artificial aging (Table 4.7). To get an estimate of the quench rate in water at 70^{o}C, the data of Zhang and Zheng [73] (Table 2.5) were plotted as shown in Fig. 5.2.

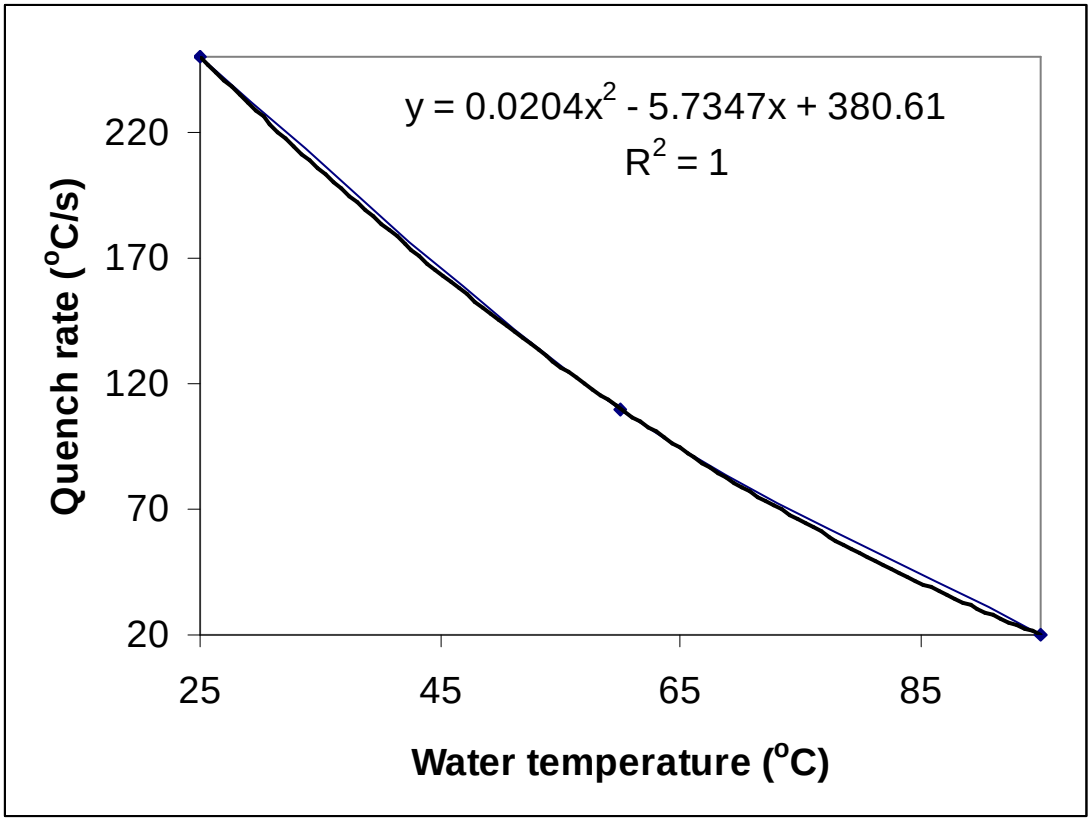

Figure 5.2: Quench rate as a function of water temperature (from [73]) for A356 samples of 14x14x55 mm^3 size.

Using the equation of the trend line in Fig. 5.2 it can be estimated that the quench rate in water at 70°C is ~ 80°C/s (note that the geometry of the plates used in this study (6x55x100mm^3) is reasonably comparable to the 14x14x55mm^3 samples used in [73]). The YS and UTS of the peak aged A356 in this study, as a function of quench rate (Table 4.7) are compared in Fig. 5.3 with those presented by Zhang and Zheng in their Fig. 2.24 [73].

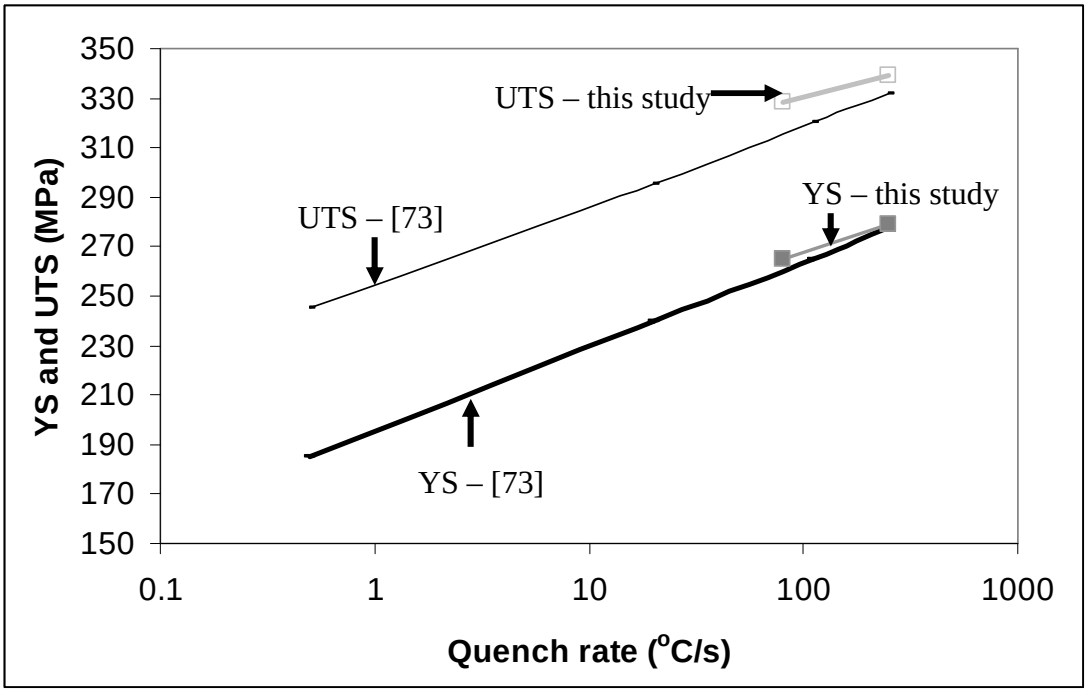

Figure 5.3: Strength of peak-aged alloy A356 as a function of the average quench rate from this study in comparison with data from Zhang and Zheng [73].

Despite the differences in microstructures (globular in this study and dendritic in [73]), the geometry of samples and artificial aging parameters (180°C-4h in this study and 170°C-6h in [73]), the effects of quench rate are very similar: the values of YS and UTS and the slopes of the curves in Fig. 5.3 correspond well. In both this study and in ref. [73] a solution treatment temperature of 540°C was used, resulting in similar solute supersaturation (the 0.40% Mg in this study and 0.38% Mg in [73] are similar) and vacancy concentration after quenching.

5.4. The T6 temper condition

It was shown that the onset of the hardness plateau (no natural aging) and hardness peak (with natural aging) in Fig. 4.18 as a function of artificial aging temperature follows an Arrhenius-type response (t_{T6} = C EXP (Q/RT)) and is described by equations 4.2 and 4.3.

$$t_{T6} = 2.3 \times 10^{-15} \text{ EXP } (163000 / 8.314T) \qquad (4.2)$$

$$t_{T6} = 4.9 \times 10^{-16} \text{ EXP } (163000 / 8.314T) \qquad (4.3)$$

An instantaneous transfer from quench to artificial aging does not have an influence on the activation energy Q of 163 kJ/mol, which is used in Chapter 6 where the artificial aging curves are modelled mathematically. However, the pre-exponential factor (C) is lower with no natural pre-aging, thereby resulting in a much faster artificial aging response. The total t_{T6} time is a complex sum of the "incubation time"+ "time of nucleation of GP zones"+ "time of growth/coarsening of GP zones"+ "time of transformation of GP zones to β″ + "time for growth and coarsening of β″. The reasons for the lower C value (and hence lower t_{T6} times) in samples that had experienced no natural pre-aging are discussed in more detail in the section on APT results (section 5.8), but in short is due to the much faster formation of GP zones and β″ owing to a high concentration of quenched-in vacancies.

The main advantage of equation 4.2 (Table 4.11) is that artificial aging times at temperature can be calculated that will result in similar tensile properties being obtained, regardless of the natural pre-aging time period. For instance, ASTM Standard B969-10 specifies that SSM-processed A356 should be artificially aged at 160^{o}C for 3-6 h to obtain the T6 temper condition (Table 2.6). However, Table 4.11 of this study (equation 4.2) shows that at 160^{o}C, a time of 29 h would be required to obtain peak properties, which also simultaneously gives similar properties in this alloy regardless of natural pre-aging. This is illustrated graphically in Figure 5.4, which shows artificial aging curves of SSM-HPDC alloy A356 (0.34% Mg) at 160^{o}C following no or 120 h natural pre-aging. Using the specified times of 3-6 h according to ASTM B969-10 will result in a large variation in tensile properties in the different naturally pre-aged alloys, in contrast to when a time of 29 h (according to Table 4.11) is used. According to this study, the specified times to achieve the T6 condition at 160°C in ASTM B969-10, probably need to be revised.

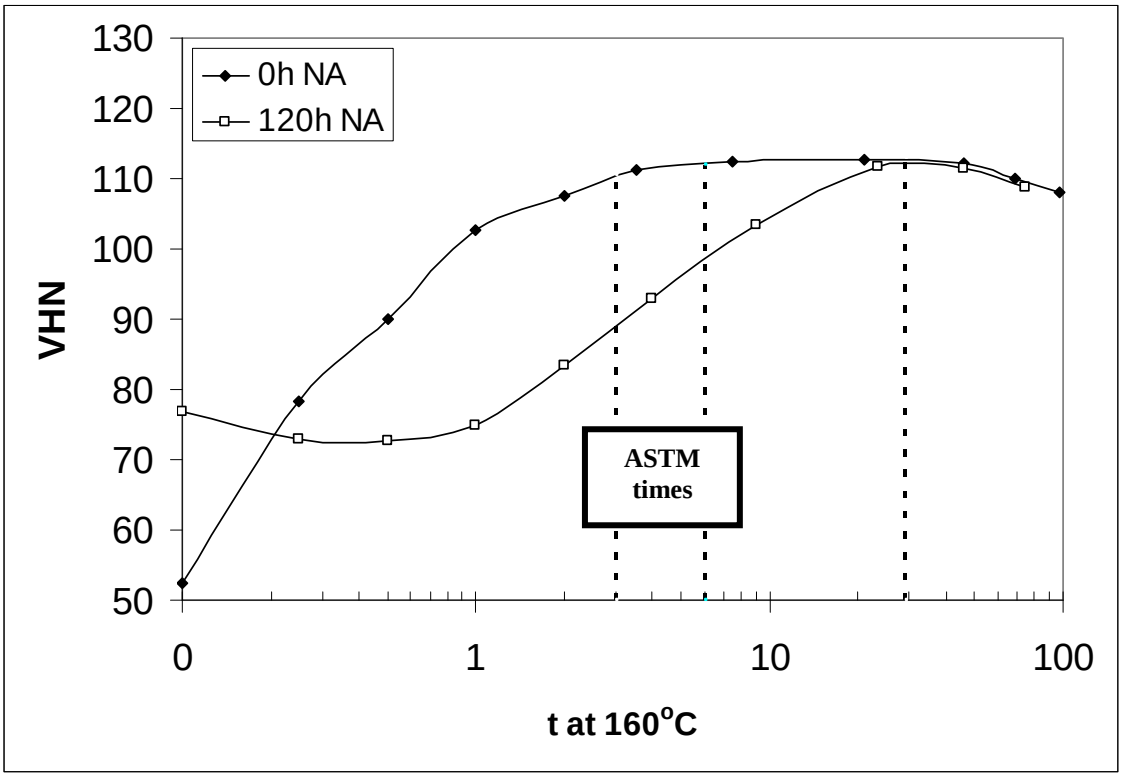

Figure 5.4: Artificial aging curves of SSM-HPDC alloy A356 (0.34% Mg) at 160°C following no or 120 h natural pre-aging, showing specified aging times of 3-6 h according to ASTM B969-10, as well as 29 h according to Table 4.11.

An artificial aging time of 29 h may be prohibitively long and therefore artificial aging parameters of 180°C for 4 h (Table 4.11) are suggested as the optimum for SSM-HPDC alloys A356 and F357 (Fig. 4.18) and for dendritic A356 and F357 (Figs. 4.60 and 4.61). The tensile properties that can be obtained using these parameters are compared with those specified by ASTM B969-10 (Table 2.9) for mid-range compositions of SSM-processed alloys A356 and F357 in Table 5.1. It is seen that the specified tensile properties are met or in most cases exceeded by using the suggested 180°C-4h T6 heat treatment cycles.

Table 5.1: Mid-range mechanical properties for rheocast A356 (0.35% Mg) and A357 (0.55% Mg) in T6 temper condition according to ASTM B969-10 and the results found in this study for SSM-HPDC A356/F357.

Alloy	Temper	0.2% YS (MPa)	UTS (MPa)	% Elongation
A356	T6-ASTM B969-10	235	310	11
A356-0.31% Mg	540^{o}C-1h, (20-120)h NA,180^{o}C-4h	254	313	10.5
A357	T6-ASTM B969-10	290	345	6
F357-0.49% Mg	540^{o}C-1h, (20-120)h NA,180^{o}C-4h	303	356	10.6

The high %elongation after fracture of the SSM-HPDC alloy F357-0.49% Mg in Table 5.1 merits further discussion. In general, the ductility of F357 is lower than that of similarly heat treated A356 (Table 4.14) due to the presence of the π-phase (Fig. 4.22). The F357 alloy in Table 5.1 used in this study was produced with a 130 ton clamping force HPDC machine, whereas the A356 was produced with a 50 ton clamping force machine. The higher intensification pressures that could be applied with the bigger machine most likely caused a reduction in microporosity compared with the smaller machine. Microsporosity in these alloys are known [103] to have a significant influence on ductility and UTS, but not much on YS and therefore the good linear graph in Fig. 4.58 is still found regardless of the casting machine used.

5.5. The T5 temper condition

The tensile properties of differently T5-treated samples of SSM-HPDC alloy F357 (with 0.63% Mg) are compared in Table 4.16. From this Table it can be seen that slightly better T5 tensile properties are obtained by water quenching the alloy after SSM-HPDC rather than cooling in air. For these experiments, a 50 ton clamping force Edgewick HPDC machine was used and a relatively long intensification time of 30s was applied before the plate castings could be quenched in water or cooled in air. The average cooling rates achieved within different parts of the plate-casting between 0-10s, 10-20s and 20-30s are shown in Fig. 4.4. Even though fast cooling rates are achieved within the plates during the first ten seconds of intensification, the cooling

rate drops significantly thereafter. Ideally, to have achieved the maximum effects of water quenching after casting, an intensification time of only 10s should rather have been used, especially considering that solidification within the plate is predicted to be complete after only ~ 5.5 s (Fig. 4.2(a)).

From Table 4.16 it can also be seen that the air-cooled T5 sample's tensile properties have significantly higher standard deviations than the water quenched T5 samples. For example, the standard deviations for the YS, UTS and %elongation for the AQ, 120h NA,180^{o}C-4h samples are 9.9, 10.9 and 1.5 respectively. This is significantly higher than the standard deviations for the YS, UTS and %elongation for the WQ, 120h NA,180^{o}C-4h samples of 1.9, 4.9 and 1.0 respectively. Considering Fig. 4.3, it can be seen that the large volume of the biscuit causes a heterogeneous temperature distribution throughout the plate casting, which would be present for longer times in the air-cooled T5 sample. This is most likely the cause of the high variation in tensile properties for this sample in Table 4.16.

The presence of β-Mg_2Si in both the F(AQ) and F(WQ) samples are shown in Fig. 4.39. The solution treatment of the T6 temper condition dissolves this β-Mg_2Si phase and the supersaturation of solute is significantly higher, which results in the artificial aging response for the T6 temper (e.g. Fig 4.18) being considerably more pronounced than for the T5 temper (Fig. 4.40). According to Fig. 2.23, the "nose" of the T-t quenching diagram for alloy F357 lies at approximately 350^{o}C and 10 s. The ProCAST simulation of Fig. 4.3 reveals that a temperature of 350^{o}C is only reached in the plate after approximately 15 s (Fig. 5.5), resulting in the precipitation of β-Mg_2Si as shown in Fig. 4.39.

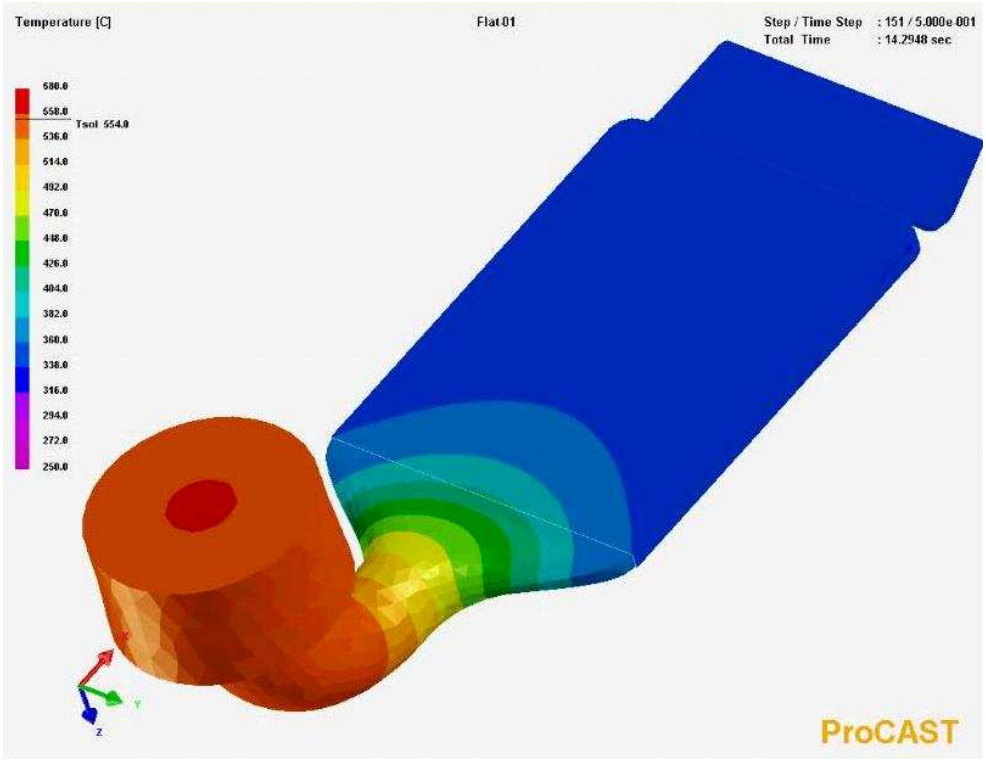

Figure 5.5: ProCAST simulation showing that the critical temperature of 350°C (Fig. 2.23) is reached in the plate during SSM-HPDC after ~ 15 s.

5.6. Comparison of aging response of globular and dendritic Al-7Si-Mg alloys

Birol [13,14], using DSC (Fig. 2.35) and artificial aging curves (Fig. 2.36), showed that there are no differences between the age hardening response of dendritic and globular Al-7Si-Mg alloys. The artificial aging curves of dendritic and globular A356 in this study (Figs. 4.60 and 4.61), as well as tensile results in Table 4.19 corroborate this conclusion. Plotting the Vickers hardness in the T6 temper condition as a function of the (at% Mg available for precipitation hardening)$^{1/2}$ in Fig. 4.62 results in an excellent linear correlation with R^2 = 0.9834. The data points in Fig. 4.62 include hardness values of A356 and F357 SSM-HPDC plates (cast with 50 ton and 130 ton clamping force HPDC machines), SSM-HPDC brake callipers (cast with a 630 ton clamping force HPDC machine), gravity die cast brake callipers with a relatively fine dendritic microstructure (Fig. 4.55(b)) and investment cast plates with a relatively coarse dendritic microstructure (Fig. 4.59). The Si-contents of the alloys used in Fig. 4.62 varied between 6.6-7.3% (Tables 3.1, 3.3, 3.4), i.e. covering almost the whole range of 6.5-7.5% allowed in the specification (Table 2.1). Figure 4.62 therefore implies that the hardness of Al-7Si-Mg alloys in the T6 temper condition is controlled

primarily by the Mg-content available for precipitation hardening after solution treatment and is independent of the casting technique used (i.e. dendritic or globular primary α-Al microstructure). The insignificant influence of Si-content variation is due to the fact that these Al-7Si-Mg casting alloys contain an excess Si that is required to form the strengthening β″–precipitates, which has a Mg:Si ratio of 1.1-1.2 (Fig. 4.79). The other important alloying element controlling the age-hardening capacity of (dendritic and globular) Al-7Si-Mg alloys is in fact iron (section 4.6). The data points in Fig. 4.62 are all for alloys containing ~ 0.1% Fe. Higher Fe-contents (especially in alloys containing > 0.40% Mg) will result in a reduced response to age-hardening due to the stability of the π-$Al_8FeMg_3Si_6$ phase (Fig. 4.22(b)). Therefore, provided that the maximum quantity of the alloy's Mg is placed into solid solution during solution treatment (which might take longer than 1 h at 540^{o}C for dendritic alloys with a very coarse dendritic microstructures such as in large sand castings), and the alloy's Fe content is within specification (but preferably ~ 0.1%), the response to age hardening of Al-7Si-Mg alloys should be independent of the processing technique used.

5.7. Comparison of aging response of SSM-HPDC Al-7Si-Mg alloys with SSM-HPDC 6000 series Al-Mg-Si wrought alloys

Both conventional casting alloys A356/7 and the conventional Al-Mg-Si 6000 series wrought alloys are strengthened by β″, but the high Si content in the casting alloys compared to the wrought alloys has a significant influence on the age-hardening response (Fig. 4.70). The solute clusters that are formed during natural aging in alloy 6082 are known to be relatively stable at the artificial aging temperature [9]. This claim is supported by the small initial decrease in hardness during artificial aging of the naturally aged 6082 sample compared to the naturally aged A356 sample in Fig. 4.70. Natural pre-aging of 6082 has an important effect on the precipitation of GP zones and β″ [84]. The atomic clusters, which formed during natural pre-aging, and the low concentration of the quenched-in vacancies in the naturally pre-aged samples, have a delaying effect upon the nucleation of GP zones. As a result, the final β″ structure developed in these 6082 samples is coarse. However, the large number of GP zones formed in the 6082 samples artificially aged without natural pre-aging, transform into a dense structure of small β″ particles, with the number density of β″

precipitates being five times higher in samples that were artificially aged immediately after solution treatment compared to samples that were naturally aged for a week before artificial aging (i.e. 200 000 vs 40 000 particles/μm^3) [84]. The opposite of these processes is believed to occur in alloys such as 6004 [9]. Chang and co-workers [50] described the positive effect of natural pre-aging on precipitation hardening in a wrought alloy with a composition similar to the 6004 in this study. They showed, in an Al-0.44at% Mg-0.38at%Si alloy, that artificial aging of naturally aged samples increased the level of the peak hardness. This was attributed to the increase in the number density of needle-like precipitates (β″) as compared to the samples without prior natural aging.

It can also be seen from Figure 4.70 that the hardening response of alloy A356 is very rapid compared to that of the wrought alloys (with the response of 6004 being the slowest). Gupta and co-workers [88] studied the precipitation hardening in wrought 6000 series alloys with and without excess Si that is required to form stoichiometric Mg_2Si. They found that excess Si (which is most pronounced in the casting alloys in this study) reduced the time to initiate strengthening, possibly due to a higher driving force for nucleation which will lead to a finer particle size and shorter diffusion distances. They also found that excess Si increases strength in both the T4 and artificially aged tempers (T6), most likely due to a higher volume fraction of strengthening precipitates as well as from a finer particle size from the higher driving force for nucleation. This is also applicable to Fig. 4.70, where alloy A356 has higher hardness values than alloy 6004, even though A356 contained 0.36% Mg compared to the 0.45% Mg of the 6004. Low hardness values for wrought alloy 6004 upon aging have been reported before [122]. Gupta and co-authors [88] claimed that the improvements to the aging response due to excess Si were caused by enhanced precipitation of fine, uniformly distributed β″ particles. They also claimed that excess Si reduced the Mg/Si ratio in the zones/clusters and β″-precipitates, thus allowing higher levels of precipitation and strengthening. From Figure 4.70 it is evident that over-aging also occurs faster in A356 than the wrought 6000 series alloys. Especially alloy 6004 maintained its maximum hardness for a long time at 180^{o}C. Gupta and co-workers [88] determined that excess Si reduced the peak strength stability in the over-

aged conditions. The reduced Mg/Si ratio is believed to make the β″ phase less stable, and as a result, the stability in strength beyond the peak aging condition is reduced.

5.8. Nanostructural evolution during aging of Al-7Si-Mg alloys

The nanostructural evolution of Al-7Si-Mg alloys as studied by means of APT and TEM (section 4.14) allows the quantification of the precipitation sequence of Al-7Si-Mg alloys, while also considering the effects of natural pre-aging.

5.8.1. Artificial aging with natural pre-aging

The T4 sample (Fig. 4.75(a)) has a large number density (2.3 x 10^{24} m^{-3}) of solute clusters containing n = 10-20 solute atoms with few GP zones (5.4 x 10^{23} m^{-3}) and no β″-needles (Fig. 4.78(a)). Figure 4.78(a) also shows that the 120h NA,180^{o}C-10min sample has a slightly lower number density (2.2 x 10^{24} m^{-3}) of solute clusters than the T4 sample, but also a marginally higher number density of GP zones (6.7 x 10^{23} m^{-3}) and no β″-needles. This suggests that the 10 min artificial aging at 180^{o}C may have resulted in the dissolution of some of the solute clusters (< 20 solute atoms), with concurrent nucleation of some new and growth of all of the GP zones (> 20 solute atoms), which results in a small decrease in macrohardness (Fig. 4.72), YS and UTS (Table 4.23). Dissolution of room temperature clusters with artificial aging has been inferred from DSC before (Fig. 2.33). However, dissolution of a large number of clusters should result in an increase in Mg and Si concentrations of the matrix after 10 min at 180^{o}C. As shown in Fig. 4.77, however, no significant changes were measured with Mg and Si essentially remaining constant at 0.51 to 0.52at% and 1.48 to 1.46at% respectively. Therefore, it is more likely that the observed nanostructural change may be due to coarsening of some small solute clusters as was also postulated before for alloy 7050 [123]. The 120h NA,180^{o}C-1h sample has less clusters (1.5 x 10^{24} m^{-3}) and more GP zones (9.5 x 10^{23} m^{-3}) than the 120h NA,180^{o}C-10min sample (2.2 x 10^{24} m^{-3} clusters and 6.7 x 10^{23} m^{-3} GP zones respectively), indicating further growth of clusters to GP zones during this artificial aging time period. Also, in contrast to the T4 and 120h NA,180^{o}C-10min samples where no β″-needles were found, the 120h NA,180^{o}C-1h sample has 1.2 x 10^{23} m^{-3} small β″-needles with n = 100 – 1200 solute atoms, but no β″-needles with n > 1200 solute atoms (Fig. 4.78(a)). This corresponds to a higher hardness and strength, as seen in Fig. 4.72 and Table 4.23. Further

artificial aging to peak hardness (Fig. 4.72) after 4 h at 180°C results in a significant decrease in solute clusters (4.3 x 10^{23} m^{-3}) and GP zones (1.6 x 10^{23} m^{-3}) compared to the 120h NA,180°C-1h sample. However, the number density of β″-needles needles is concurrently increased, with large needles containing > 1200 solute atoms (4.3 x 10^{22} m^{-3}) found in this sample resulting in peak strength (Table 4.23). Heterogeneous nucleation of β″-needles from GP zones has been postulated before [43,84].

5.8.2. Artificial aging without natural pre-aging

The 0h NA,180°C-10min sample has a high number density of solute clusters (2.2 x 10^{24} m^{-3}) and GP zones (1.3 x 10^{24} m^{-3}), with a lower number density of small β″-needles with n = 100-400 solute atoms (7.6 x 10^{22} m^{-3}) (Fig. 4.78(b)). This is in good agreement with the faint streaks observed in the <001> SADP of the sample (Fig. 4.74(a)) as discussed previously. Further artificial aging to 1 h at 180°C caused a decrease in the number density of both solute clusters (8.3 × 10^{23} m^{-3}) and GP zones (5.4 × 10^{23} m^{-3}), with a concurrent increase of this number in small β″-needles containing 101-1200 solute atoms (3.3 × 10^{23} m^{-3}) and large β″-needles with n > 1200 in a low number density of 2.4 × 10^{21} m^{-3}. With the increase in aging time from 1 h to 4 h at 180°C, the number density of solute clusters decreases almost 12 times to 7.3 × 10^{22} m^{-3} and that of GP zones more than 6 times to 8.5 × 10^{22} m^{-3}. Concurrently, the number density of large β″-needles with > 1200 solute atoms increased almost 8 times to 1.9 × 10^{22} m^{-3} (Fig. 4.78(b)). This coincides with the hardness plateau as shown in Fig. 4.72. During coarsening of the β″-precipitates within the hardness plateau, both the UTS and macrohardness values remain relatively constant, but the YS increases (Table 4.23).

5.8.3. Comparison of artificial aging with and without natural pre-aging

The 120h NA,180°C-10min and 0h NA,180°C-10min samples have similar number densities of solute clusters, but the latter sample has a significantly higher number density of GP zones and also contains small β″-needles with n = 100-400 solute atoms (Fig. 4.78). The vacancy-rich solute clusters that are formed during natural aging diminish the matrix of quenched-in vacancies [84,124]. The lower concentration of quenched-in vacancies in the 120h NA,180°C-10min sample compared to the 0h NA,180°C-10min sample most likely had a delaying effect on precipitation of GP

zones by limiting diffusion. This also agrees with the model for GP zone growth postulated by Herman [125]. The clusters are vacancy-rich due to lattice strains caused by the differences in atom radii of Al, Mg and Si of 0.143, 0.160 and 0.117 nm respectively [126], which results in misfits of +11.9% for Al-Mg and -18.2% for Al-Si. The higher number densities of GP zones and small β″-needles in the 0h NA,180^{o}C-10min sample compared to the 120h NA,180^{o}C-10min sample causes a marked increased hardness (Fig. 4.72) and strength (Table 4.23)

The 120h NA,180^{o}C-1h sample has a higher number density of solute clusters and GP zones than the 0h NA,180^{o}C-1h sample, with a concurrent lower number density of β″-needles (Fig. 4.78), which results in lower hardness (Fig. 4.72) and strength (Table 4.23).

The 120h NA,180^{o}C-4h sample has similar hardness, YS and UTS than the 0h NA,180^{o}C-4h sample (Table 4.23). However, the 120h NA,180^{o}C-4h sample has a significantly higher number density of solute clusters and GP zones than the 0h NA,180^{o}C-4h sample (Fig. 4.78). The presence of a larger number of small clusters and GP zones in the naturally pre-aged sample is most likely due to remnants of clusters and GP zones that had formed during natural aging. These would have been the room temperature clusters and GP zones that were durable during artificial aging and which did not undergo reversion. Such stability of room temperature clusters during artificial aging at 180^{o}C of Al-Mg-Si alloys has been reported before [50,86]. Yamada and co-workers [86] postulated that these clusters are Si and –vacancy rich (see section 5.9.1) and are durable at 180^{o}C due to the strong covalent bonds between the Si atoms within these clusters. The 120h NA,180^{o}C-4h sample also has a higher number density of large β″-needles with n > 1200 solute atoms than the 0h NA,180^{o}C-4h sample and a correspondingly lower number density of smaller β″-needles with n = 100-1200 solute atoms. Whereas the 0h NA,180^{o}C-4h sample therefore relies mostly on a relatively high volume fraction of comparatively small β″-needles for its hardness and strength, the 120h NA,180^{o}C-4h sample relies more on a combined presence of solute clusters, GP zones and large β″-needles.

After aging for 4 h at 180°C, the relative reductions of the matrix solute concentrations detected in the two samples reached the same level, which indicates that the decomposition of the supersaturated solid solution in the two respective microstructures has developed to a similar stage (Fig. 4.77). The initial vacancy concentration difference between the two samples therefore has little influence on the long-term precipitation process after 4 hour aging. After 1 h aging at 180°C, the vacancy concentrations of the two samples appear to have quickly evolved to the stable concentration at that temperature.

5.9. Characteristics of precipitates in Al-7Si-Mg alloys

5.9.1. Solute clusters

The solute clusters are fully coherent with the matrix and cannot be resolved by TEM (Fig. 4.73(a)). They are Si-rich with a Mg:Si ratio of less than the theoretical 0.83 of β″ (Fig. 4.79). Rinderer and co-workers [11] showed that the clusters in under-aged A356 have a Mg:Si ratio of 0.7, which is in good agreement with the results in this study. The clusters are enriched in Si [80,86] due to its higher diffusion rate and lower solubility than Mg in Al [39,50]. The strong covalent bonds between the Si atoms in the clusters presumably make them durable at artificial aging temperatures of 180^{o}C, even at a time of 4 h that corresponds to the peak aged condition.

5.9.2. GP zones

The GP zones are approximately 2 nm in diameter and can be resolved by TEM in Fig. 4.74(a). GP zones are fully coherent with the matrix and do not have a distinct structure and therefore their SADP's (Fig. 4.74(a)) do not show extra reflections nor diffuse scattering. The Mg:Si ratio of GP zones of 0.8-1.1 (Fig. 4.79) is higher than those of the solute clusters and are close to the theoretical value of 0.83 of β″. The increase in Mg-content of the GP zones compared to clusters indicates that Mg-diffusion is rate limiting during precipitation [80]. Using the Arrhenius parameters from Du and co-authors [105], it can be calculated that the diffusivity of Mg in Al at 180^{o}C is half of that of Si in Al (1.9 x 10^{-19} and 3.8 x 10^{-19} m^2/s respectively).

5.9.3. β″-needles

The β″-needles range in size from ~ 2 nm diameter x 10 nm length early during artificial aging (Fig. 4.73(c)) to ~ 4 nm diameter x 25 nm in the peak aged condition (Fig. 4.73(d)). The β″-needles have the highest Mg:Si ratio of all the precipitates due to the precipitation process being controlled by Mg-diffusion (Fig. 4.79). The needles with > 1200 solute atoms for instance have a Mg:Si ratio of ~ 1.0–1.2 (more than 0.83 of β″ but less than 1.7 of β′) - in excellent agreement with the ratio of 1.2 found by Rinderer and co-workers [11] for peak aged β″-needles in alloy A356. Recent first principle calculations suggest that the lowest formation enthalpy configuration of β″ has a Mg:Si ratio of 1.25 [127].

5.10. Precipitation sequence of Al-7Si-Mg alloys

By considering the results obtained by employing TEM and APT in this study, the precipitation sequence can be expressed as follows, while also elucidating the co-existence of precipitates during precipitation.

- **During natural aging (T4)**: Formation of a high number density of vacancy- and Si-rich Si-Mg clusters with a significantly lower number density of GP zones and no β″-needles.
- **During artificial aging after natural pre-aging**: Coarsening of the room temperature clusters → spherical GP zones → β″-needles, coinciding with a decrease of the matrix Mg and Si content and an increase in Mg:Si ratio of the precipitates, while retaining a relatively high number density of room temperature Si-rich clusters and GP zones that remain durable during artificial aging.
- **During artificial aging without natural pre-aging**: A high concentration of solute and quenched-in vacancies leads to rapid formation of clusters and GP zones → relatively small β″-needles at the start of the hardness plateau → coarsening of β″-needles during the hardness plateau depleting the matrix from Mg and Si, increasing the Mg:Si ratio of the precipitates, whilst retaining only a few clusters and GP zones, which results in constant hardness and UTS, but increasing YS.

Summary: SSS → solute clusters → solute clusters + GP-zones → solute clusters + GP-zones + $\beta''_{needles.}$

A natural pre-aging treatment has a significant influence on the precipitation kinetics during initial 1 h artificial aging of alloy F357. Natural pre-aging, however, has no influence on the precipitation sequence, but it affects the relative proportion of solute clusters, GP zones and β″-needles.